MICROSCOPY

Microscopy, 2018, i3–i13
doi: 10.1093/jmicro/dfx130
Advance Access Publication Date: 23 January 2018

Article

Excitation of long-wavelength surface optical vibrational modes in films, cubes and film/cube composite system using an atom-sized electron beam

Maureen J. Lagos[1,2,3,*], Andreas Trügler[4,*], Voshadhi Amarasinghe[3], Leonard C. Feldman[1,2,3], Ulrich Hohenester[4], and Philip E. Batson[1,2,3]

[1]Department of Physics and Astronomy, [2]Department of Materials and Science Engineering, Rutgers University, Piscataway, NJ 08854, USA, [3]Institute for Advanced Materials, Devices, and Nanotechnology, Rutgers University, Piscataway, NJ 08854, USA, and [4]Institute of Physics, University of Graz, Universitätsplatz 5, Graz 8010, Austria

[*]To whom correspondence should be addressed. E-mail: lagos.maureen@gmail.com (M.J.L) and andreas.truegler@uni-graz.at (A.T)

Received 18 August 2017; Editorial Decision 8 December 2017; Accepted 16 December 2017

Abstract

Using spatially resolved Electron Energy-Loss Spectroscopy, we investigate the excitation of long-wavelength surface optical vibrational modes in elementary types of nanostructures: an amorphous SiO_2 slab, an MgO cube, and in the composite cube/slab system. We find rich sets of optical vibrational modes strongly constrained by the nanoscale size and geometry. For slabs, we find two surface resonances resulting from the excitation of surface phonon polariton modes. For cubes, we obtain three main highly localized corner, edge, and face resonances. The response of those surface phonon resonances can be described in terms of eigenmodes of the cube and we show that the corresponding mode pattern is recovered in the spatially resolved EELS maps. For the composite cube/substrate system we find that interactions between the two basic structures are weak, producing minor spectral shifts and intensity variations (transparency behaviour), particularly for the MgO-derived modes.

Key words: surface optical phonons, vibrational EELS, vibrational scattering cross-section, surface phonon polariton, infrared terahertz

Introduction

Finite systems sustain surface optical vibrational modes [1–3] whose properties are driven by the system shape and size. These modes play an important role in a large variety of nanoscale phenomena, such as light-phonon coupling [4], radiative heat transfer [5], heat and sound flow [6], van Der Waals friction [7], Casimir forces [8], among others. A deeper understanding of these phenomena requires fundamental experimental studies of the physical properties of surface vibrational modes in isolated nanosized objects

with high spatial resolution. In particular, experimental studies using local probes, which allow the excitation of highly localized surface and bulk vibrational modes [9] in single nanosized objects of different shapes and sizes, can provide valuable information useful for the design of more efficient infrared low-loss nanophotonic devices [10], nanophononic thermal devices [11], novel thermophotovoltaic devices [12], etc.

Nanosized structures can sustain several kinds of vibrational surface modes. For instance, a surface phonon mode in a semi-infinite flat surface was predicted by Fuchs and Kliewer (FK) [13]. This mode is a longitudinal confined charge density wave oscillating along the surface with an angular frequency defined by the equation $\varepsilon(\omega) = -1$, where ε is the bulk dielectric function within the structure. Also, for a thin slab of finite thickness, two different surface modes are generated due to the coupling between surface charges in each side of the slab surfaces through internal electric fields [14]. These self-sustained modes are the so-called *surface phonon polaritons* (SPhP) [2] and they will be further discussed in this work. More interestingly, the *shape* of the nanoscale structure plays a fundamental role in tuning the frequency of surface phonon modes, and so, for instance, Fröhlich proposed that a surface confined phonon mode in an ionic sphere would have a resonant frequency defined by the relation $\varepsilon(\omega) = -2$ [15]. Also, Fuchs [16] pointed out the existence of long-wavelength polariton optical modes in ionic cubes, whose eigenmode resonances could be identified $\varepsilon(\omega) < 0$. Finally, several theories of surface optical phonons for objects having *arbitrary shapes* were also introduced [1,16,17]. In addition, the study of SPhP coupling effects between neighbouring phononic nanostructures remains to be further explored. All these localized surface optical phonon modes can be excited using external light and charge probes with efficiencies governed by how well the external probe matches the local size, directionality or symmetry of possible modes, defining *selection rules* for scattering processes.

Due to limits in the spatial resolution of vibrational spectroscopy techniques, most experimental studies of such confined surface vibrational excitations have been limited to large surface areas, micrometre-sized structures and large ensembles of nanostructures/molecules. Spectroscopic studies that provide spatially resolved information about the physics of those surface excitations in isolated nanostructures still largely remain to be performed in the future. Recently, atom-sized electron probes fabricated in electron microscopes were filtered in energy resulting in electron beams having a few meV of energy spread [18]. These now allow the detection of excitations in the infrared range down to 50 meV [9], and to resolve SPhP excitations spaced apart by ~14 meV in boron nitride flakes [19]. Using these remarkable capabilities, spatially resolved vibrational studies of nanostructures have began opening the door for further exploration of vibrational properties in isolated nanostructures with nanometric resolution.

Electron beams can probe the spectrum of excitations of matter. Because the response of a system probed by a single keV electron is linear, this response is fully determined by the system properties in the absence of the external beam. In particular, spatially resolved electron energy loss spectroscopy (EELS) allows the mapping of inelastic scattering due to specimen excitations such as plasmons and phonons [9,20–22] in nanostructures with high spatial resolution.

In these experiments, we describe the inelastic electron scattering within the local dielectric formulation. In the long-wavelength limit ($q \to 0$), keV energy electrons are deflected by small angles as a result of the small amounts of momentum transferred during the scattering. Experimentally, we can restrict scattering to long wavelengths by using a non-intersecting beam-specimen geometry or by using small apertures located near the optic axis of the microscope to restrict the angular content of the incident and scattered electrons [9,18,23–26]. Theoretically, the semi-classical dielectric theory is able to give a good description of this case, and indeed, most of the knowledge acquired about surface plasmons in nanostructures by electron scattering can be applied to interpret data of infrared phonon excitations as well. However, careful attention must be paid to ensure the validity of the theoretical methods and to avoid known situations where the local dielectric approach fails [27,28]. In this scenario, additional experimental data are required to test new theoretical models and ideas.

In this paper, we present a study of the excitation of long-wavelength optical surface vibrational modes in two elementary phononic systems which exhibit surface phonon modes: amorphous silicon dioxide (a-SiO_2) nanometric films and magnesium oxide (MgO) nanocubes. We explore in detail the scattering process of a fast electron with confined surface vibrational excitations in nanostructures in the dipole limit ($q \to 0$). Surface phonon excitations in thin films have been extensively studied using many techniques, including EELS in the reflection geometry (R-EELS), and the physics of surface dipolar excitations is extensively documented [3]. Our study here focuses on the excitation of SPhP modes in the transmission geometry [29], exploring the excitation of modes which remain inactive when probing the slab in the reflection geometry. Furthermore, we performed spatially resolved vibrational studies of localized surface phonon excitations in isolated MgO nanocubes in similar manner as in [9], and in addition, we include a more detailed theoretical analysis of those localized surface excitations. We present experimental results acquired in the

aloof geometry, thus naturally exciting long-wavelength modes in the dipole limit. The inelastic scattering from surface vibrational modes for slabs and cubes is described in terms of excitation of eigenmodes within the dielectric formalism. Finally, we considered a composite system combining these two nanostructures to create a system consisting of one MgO cube sitting on a thin *a*-SiO_2 substrate.

Methodology

We grew *a*-SiO_2 films on [100] sodium chloride (NaCl) crystals using a Plasma-Therm 790 PECVD system at ~10 nm/min and 250°C. The oxide thickness was calibrated by depositing on a piece of silicon under the same conditions and measuring the thickness using optical ellipsometry. After the deposition, the process chamber was cooled down to room temperature and the silica film was floated off the substrate onto the surface of de-ionized water and captured on a TEM grid.

We deposited MgO nanocubes onto a lacey amorphous carbon microscopy grid by collecting the combustion smoke from burning a magnesium ribbon in air. In this process, we do not have control over the size of the produced nanostructures, and we usually obtain a broad size distribution of suspended cubes, ranging between 30 and 500 nm in size. The smoke cubes are single crystal with very flat faces.

We conducted vibrational EELS experiments following the procedure described in reference [9]. Briefly, we used a Nion UltraSTEM microscope equipped with both a monochromator and an aberration corrector operating at 60 kV. A probe of 30 mrad convergence semi-angle with a beam current of ~5–10 pA was used, producing a probe size of ~1.5–2 Å with 10–12 meV wide energy distribution. The EELS spectrometer entrance aperture subtends ~20 mrad half angle.

Calculations of the vibrational response were performed using the dielectric approach. Scattering cross-sections for the thin slabs were calculated including retardation effects within the local dielectric response [30,31]. The EELS simulations for the MgO nanocubes and the composite system MgO/SiO_2 were performed using the MNPBEM (Metallic NanoParticles Boundary Element Method) toolbox [32]. In this approach, the calculation of physical quantities (response electric fields, surface charges, scattering probabilities) associated with the electron energy loss follows the methodology in reference [33]. The basic idea behind the boundary element method is the formulation of Maxwell's equations in terms of surface integrals and seeking their numerical solution through a discretization of the involved surfaces into small boundary elements. With our implemented simulation tool, we can study the plasmon/phonon response of nanostructures in terms of their (degenerate) eigenmodes, analyse the surface and bulk contributions to the loss function, and perform calculations as a function of collection conditions. An experimentally determined dielectric function for *a*-SiO_2 and MgO [34] that only depends on the frequency is used as an input parameter. The validity of our approach in the infrared range is confirmed by the good agreement between calculations and reported experimental data [9]. A quantitative comparison of scattering cross-sections however was not attempted.

Since the calculation of the dielectric response requires the knowledge of the dielectric function of the material, it will be helpful for our description to highlight a few characteristics of the dielectric function of MgO and *a*-SiO_2 in the long-wavelength range ($q \rightarrow 0$). Both materials are considered to exhibit ionic behaviour, even silica whose chemical bonds are ~50% ionic [35]. Typical dielectric functions of ionic crystals are usually described by a single Lorentz oscillator (Fig. 1a) or a set of oscillators (Fig. 1b). Figure 1a shows the dielectric function of a bulk MgO crystal using one single IR active optical mode. The resonance frequency of the bulk system is given by the transverse optical (TO) phonon mode at ~50 meV. The other resonance frequency corresponds to the longitudinal (LO) optical frequency at ~90 meV. In the limit ($q \rightarrow 0$), those optical modes involve the displacement of the oxygen sub-lattice against the magnesium sub-lattice. The TO and LO frequencies define a region ($\omega_{TO} < \omega < \omega_{LO}$) called the *Restrahlen* band, where $\mathrm{Re}[\varepsilon] < 0$, indicated by the light grey in Fig. 1a. The bandwidth (50 meV < ω < 90 meV) is ~40 meV.

In similar manner, the dielectric response of SiO_2 exhibits two independent Lorentzian oscillators producing two *Restrahlen* bands which are separated by one bulk optical phonon instability at around 100 meV (Fig. 1b). The upper and lower bands are narrower and have a width of ~8 and 20 meV, respectively. Following the nomenclature established by the IR community, we label the transverse optical resonances as TO_1 (55 meV), TO_2 (100 meV) and TO_3 (135 meV) [36]. The attribution of those resonances to specific molecular modes of the Si–O–Si bonds is well established [37]. Briefly, the TO_1 mode is identified as rocking mode of the oxygen atoms, perpendicular to the Si–O–Si plane. The TO_2 is assigned to a stretching mode of the oxygen atom along a line bisecting the Si–O–Si angle, including a simultaneous movement of the Si ions. The TO_3 anti-symmetric stretching mode involves the motion of the oxygen atom along a line parallel to the Si–Si axis.

Furthermore, it is well known that terminating the bulk crystal by a surface breaks the translational symmetry and leads to the generation of a third resonance [38]. The surface mode frequencies follow the condition that the real part is negative ($\mathrm{Re}[\varepsilon] < 0$), thus implying that all the

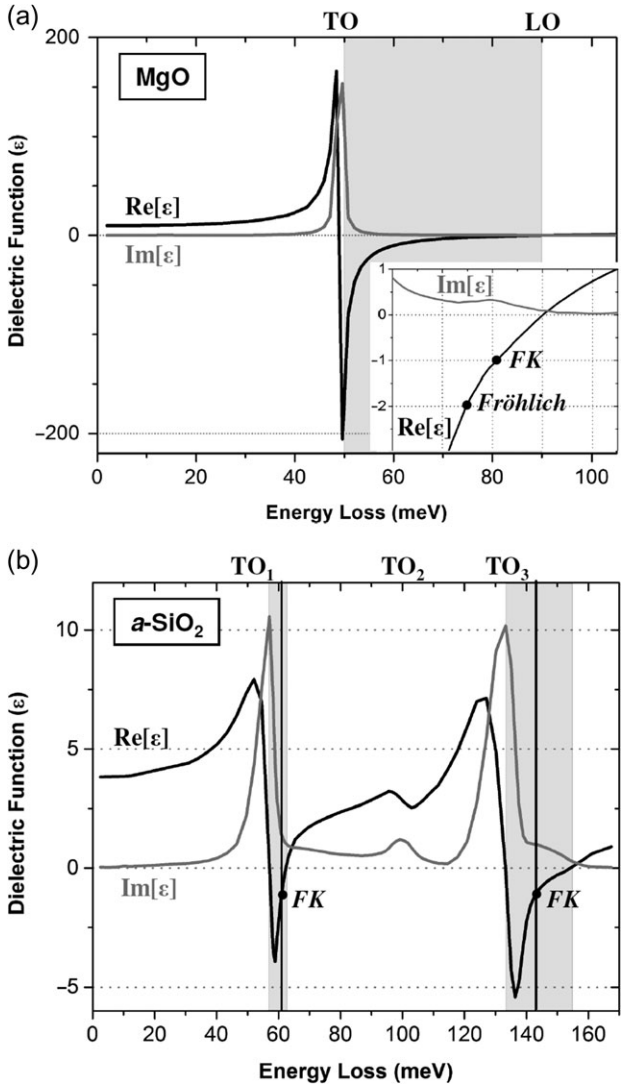

Fig. 1. Experimentally determined dielectric functions of bulk (a) MgO and (b) *a*-SiO_2 in the long-wavelength limit ($q \rightarrow 0$). The continuous black and grey curves represent the real (Re[ε]) and imaginary (Im[ε]) part of the function, respectively. (a) The dielectric response of MgO is represented by a single Lorentzian oscillator describing a single active infrared mode. The transverse (TO) and longitudinal (LO) optical modes are identified at the crossover of the real part (Re[ε] = 0) and they form the limits of the *Restrahlen* band indicated by the grey area. The inset shows a magnified view of the region between 60 and 110 meV, indicating the condition for the excitation of surface phonon Fuchs-Kliewer (FK) (Re[ε] = −1) and Fröhlich (Re[ε] = −2) modes. (b) The dielectric response of *a*-SiO_2 is represented by two Lorentzian oscillators separated by a bulk phonon instability at ~100 meV. Two *Restrahlen* bands are generated indicated by the grey regions. The corresponding transverse optical excitations are denoted by TO_1, TO_2 and TO_3. The vertical black lines within each band indicate the energies of the FK mode.

surface optical resonances lie in the *Restrahlen* band of the material. For instance, the FK surface frequency of a semi-infinite flat MgO slab is given by the condition ε equals to −1, producing a resonance at ~82 meV [39], while the lowest Fröhlich frequency of a MgO sphere is ~74 meV, at ε equals to −2 (see inset Fig. 1a). Note that for this energy range, the imaginary part of the dielectric function (Im[ε]) is very small, which implies that surface phonon excitations have small dissipation. This particular characteristic reflects on the high *Q*-factors of dielectrics, which represents the rate of energy loss with respect the stored energy of an oscillator [10]. It is indeed an important property of materials for the development of efficient low-loss nanophotonic devices.

Results and discussion

Amorphous SiO_2 thin film

Figure 2a shows two background-subtracted vibrational EELS spectra of *a*-SiO_2 thin films of ~40 and 100 nm in thickness. Three main energy-loss resonances appear in each spectrum and their scattering strength scales with the film thickness. The strong resonances located at ~55 and 135 meV in each spectrum correspond to the excitation of self-sustained SPhP modes in the films, as we will discuss below. Each one of these resonances lies in a *Restrahlen* band of the material (see Fig. 1b) and their exact position and shape is governed by the film thickness. For instance, note that the resonance obtained for the 30 nm film is at 135 meV and shifts towards 140 meV for the 100 nm film. The shift of the resonances in the lower band is minor. We also found a third resonance at ~100 meV which corresponds to the excitation of a bulk vibrational mode and its position does not depend on the film thickness. Those three optical resonances are associated with specific molecular modes of the Si–O–Si groups that we discussed above [37]. Our experimental results are in good agreement with previous results reported in the literature using photon techniques, such as IR [36] and inelastic x-ray spectroscopy (IXS) [40].

We describe our results based on the local dielectric response of an ionic slab. In the long-wavelength limit, the dielectric slabs sustain SPhP's and two different optical modes appear due to the coupling between the charges on the slab surfaces [3]. An extensive description of those SPhP excitations in an ionic slab of a single infrared active optical is presented in the first section of the Supplementary data (Fig. S1). In similar manner, based on the description of SPhP's excitations in slabs, we expect two different branches of SPhP's (FK^+ and FK^-) excited within each *Restrahlen* band, on either side of the vibrational bulk mode at ~100 meV. Figure 2b shows two-dimensional plots of the double differential scattering probability for SiO_2 slabs of different thicknesses at zero kelvin. The plots on the left and the right side were calculated considering silica slabs of 20 and 120 nm in thickness, respectively. Within each *Restrahlen* band, we observe that the symmetric nonradiative

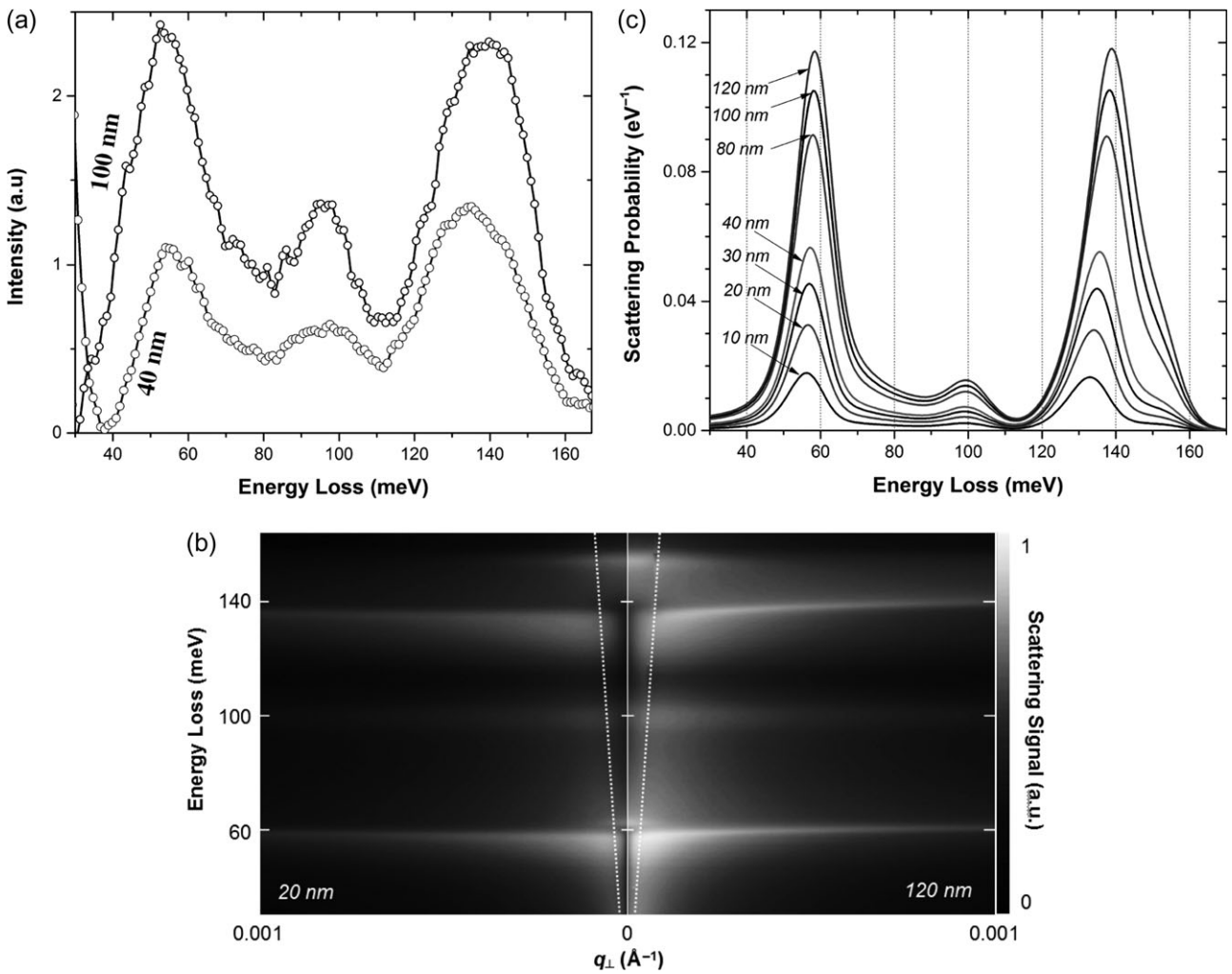

Fig. 2. (a) Background-subtracted vibrational EELS spectra for *a*-SiO_2 films of ~100 and 40 nm in thickness. Three main resonances are observed at ~55, 100 and 135 meV. (b) 2D-density plots of electron inelastic scattering from the SPhP's for a 20 nm (left side) and 120 nm (right side) slab in the long-wavelength range. In each *Restrahlen* band there are two SPhP modes (FK^+ and FK^-) and the electron couples very efficiently to the symmetric FK^- mode, as indicated by the strong signal associated with the corresponding mode. The intensity is represented in logarithmic scale and the light line is represented by a dotted line in each dispersion curve. Note that the most excited FK^- modes disperse due to film thickness, with the dispersion more pronounced for thicker films. (c) Scattering probabilities of *a*-SiO_2 films as a function of thickness. The theoretical curves were convoluted with a 12 meV width Gaussian function accounting for the instrument response. The three main resonances are in good agreement with the experimental data in (a). Note that low and high-energy resonances shift as a function of the slab thickness.

FK^- mode couples strongly to the fast electron contributing predominantly to the inelastic scattering in the transmission geometry, in contrast with results from R-EELS, which favours contributions of the FK^+ modes. The excited FK^- modes lie in the nonradiative region (right side of the light line) of the dispersion curve and they have evanescent fields which exponentially decay outside the slab. Also, note that there are optical modes on the radiative region (left side of the line light) that are excited [41].

Another important feature of the symmetric FK^- modes is their dispersion slope which is driven by the film thickness: the thicker the film, the faster the FK^- mode disperses approaching the FK frequency ($\mathrm{Re}[\varepsilon] = -1$). We expect the dispersion of the FK^- mode in the lower band to be less pronounced because it is narrower than the upper band, in agreement with the experimental data (Fig. 2a). It is also important to observe that the bulk vibrational mode ($\mathrm{Re}[\varepsilon] > 0$) around 100 meV does not disperse in energy. The scattering signal of this bulk excitation seems to be not as strong as the surface scattering signal of the FK^- modes, probably due to the small oscillating electric dipoles associated with the long-wavelength vibrational mode. However, stronger inelastic interaction with short-wavelength phonon modes can be expected for this particular mode, as noticed from inelastic scattering with x-rays [40].

To analyse the contributions of the vibrational excitations to the EELS signal, we calculated the scattering probability per energy unit, integrating the scattering signal

(Fig. 2b) through a certain solid scattering angle determined by the collection conditions. Figure 2c shows theoretical scattering probabilities for a-SiO_2 slabs of different thickness (10–120 nm). We focused on surface optical excitations in the long-wavelength range and thus we considered transmitted electrons that scattered up to small angles (12 μrad or $q_\perp = 0.0015\ Å^{-1}$). This cut-off value is equivalent to a collection condition that emphasizes excitation wavelengths larger than 4000 Å, which is a reasonable assumption for the excitation of long-wavelength excitations. Our theoretical results predict three main energy loss resonances (Fig. 2c), in good agreement with the experimental EELS results (Fig. 1a). These loss resonances contain mainly contributions from the excited FK^- modes of the slab, as discussed above (Fig. 2b). Also, note that the 55 and 135 meV loss peaks shift to higher loss energies as the thickness increases, the shift being more pronounced for the excitations in the upper band, as observed in the experimental EELS data (Fig. 2a).

In addition, theoretical analysis of the local dielectric response of silica films predict about seven times more surface scattering than bulk signal (~100 meV) in the long-wavelength limit, which represents a surface/bulk ratio value three times larger than the ratio in the experimental spectra (Fig. 2a). We believe that there is more bulk scattering (100 meV) in the experimental data due to the contribution of short-wavelength excitations collected at large scattering angles [40]. A fuller description accounting for short wavelength excitations should include the non-local dielectric response ($q \gg 0$) of the material; however, those additions should produce negligible contributions to the surface resonance amplitudes (~55 and 135 meV).

The theory of local dielectric response of silica films provides understanding on the nature of the SPhP excitations in isotropic materials. In similar way, the dielectric theory for anisotropic materials, typically used for plasmon excitations [42], can also used for the study of the phononic response of films of anisotropic materials. Several dielectric models describing the inelastic scattering processes in the reflection and transmission geometry were also presented [19,26,43].

MgO nanocubes

In contrast to the case of the slab, which only exhibits two main SPhP modes and allows any amount of momentum (q) to be transferred parallel to the surface from the electron during the scattering, cubes exhibit a large variety of eigenmodes and their finite lateral size imposes a limit in the amount of momentum transferred ($q > 2\pi/L$, where L is the cube length). In this section, we present experimental results associated with the excitation of surface optical phonon modes in the non-intersecting geometry, analysis of the vibrational scattering in terms of eigenmodes and their contributions to the scattering, and a description of the dielectric response associated with the three most important surface phonon resonances.

Figure 3a and b shows background-subtracted phonon EELS spectra for a 150 nm MgO nanocube oriented along the [001] and [110] directions, respectively. The EELS data were collected in the *aloof* geometry, as a function of impact parameter (b), and they reveal a large variety of loss peaks which depend strongly on both the probe location and the cube orientation. Those broad loss peaks can be visualized by the convoluted contribution of only three main resonances at ~69, 72 and 81 meV, which were labelled corner, edge and face modes, respectively (see black dotted curves of Fig. 5a).

Figure 3a shows spectra acquired along the [110] (upper part) and [100] (lower part) directions, respectively. For the beam located close to the cube corner ($b = 2$ nm) a loss peak shows up at ~69 meV (corner mode), which remains located at the same energy for acquisitions at large impact parameter conditions ($b = 2$–50 nm). This indicates that the corner mode is strongly excited, with smaller contributions from the edge and face modes. For the beam located close to the cube face ($b = 2$ nm) an asymmetric broad peak shows up with the maximum at ~77 meV. When the beam is displaced away from the cube the shape of the loss peak gets broader revealing two maxima, one at ~81 (face mode) and the other at ~69 meV (corner mode).

Figure 3b shows spectra acquired from one corner of the cube along two different directions: the [1$\bar{1}$0] (upper part) and [001] (lower part). The impact parameter is ~5 nm and it is measured in the direction which is perpendicular to the line of data acquisitions. For the probe located in the corner, the spectrum shows a resonance at ~69 meV (corner mode), in agreement with the results for the corner mode in Fig. 3a—upper part. As the beam moves along the [1$\bar{1}$0] direction, the spectra get broader; the spectrum maximum shifts towards higher energy values; and a shoulder is developed at ~81 meV (face mode). When the probe is displaced from the corner along the [001] direction the loss peak shifts to higher energy, reaching ~72 meV (edge mode) at the middle point along the edge. Along this line we found that the corner contributions decrease in favour of the edge contributions.

It is important to note that only three resonances associated with the excitation of surface optical modes in cubes are observed in the EELS spectra. The scattering strength of each resonance can be tuned through the impact parameter distance with respect to the particle, which results in a large variety of loss peaks, as shown in Fig. 3. Each of these three resonances (corner, edge and face) can be

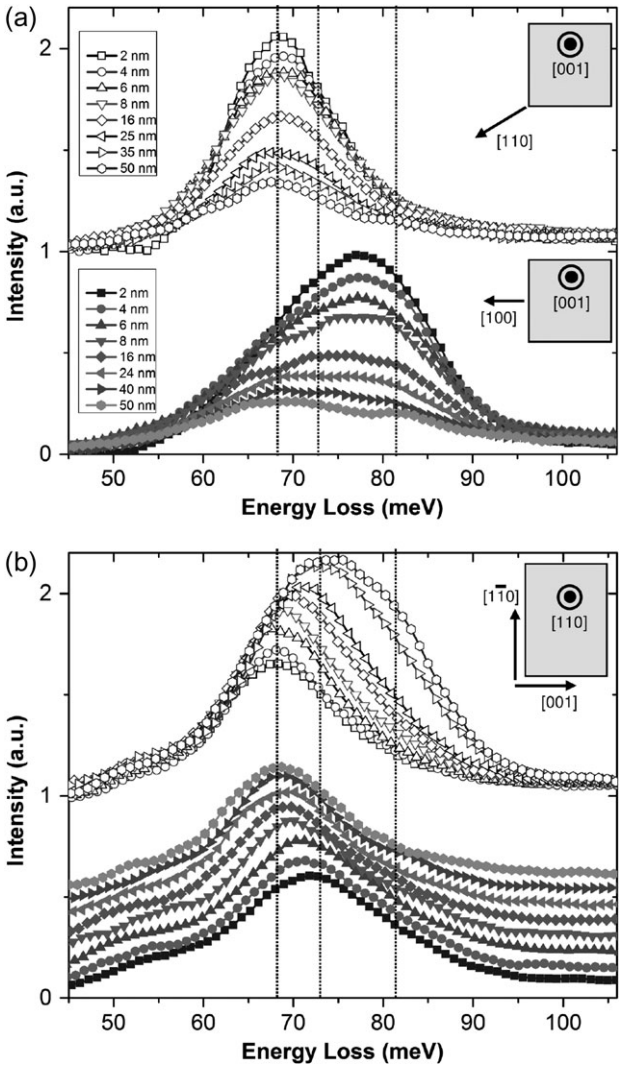

Fig. 3. Background-subtracted phonon EELS spectra for suspended MgO nanocubes of 150 nm in length oriented along the (a) [001] and (b) [110] directions. The data were acquired for different electron beam positions in the non-intersecting geometry. Three main surface resonance modes located at ~69 meV, 73 meV and 81 meV are distinguished, which are usually called corner, edge and surface modes (see vertical dotted lines). The surface scattering associated with those resonances is controlled by the impact parameter. (a) The spectra on the upper and lower part were acquired along the [110] and [100] directions, respectively, in the plane perpendicular to the incident electron direction, for impact parameter between 2 and 50 nm, respectively. The surface scattering strength decays for large impact parameter values. (b) The spectra on the upper and lower part were acquired along the [1$\bar{1}$0] and [001] directions for ~5 nm of impact parameter. A resonance at ~69 meV is found for the beam location close to the cube corner. The spectra shift to higher energy values and changes in shape when the probe is moved along the aforementioned directions. The spectra acquired along the [100] direction (lower part) were shifted in the vertical direction to render a better visualization. See text for explanation.

described in terms of eigenmodes [44], in similar manner as presented by Fuchs [16]. In the quasi-static regime, the eigenmode expansion of a nanoparticle's response is rather straightforward and can be described by a simple expression, where the geometric information of the investigated system is decoupled from the material properties [45]. Thus, the quasi-static eigenmode solutions are solely connected to the particle geometry and the final contribution of each eigenmode is determined by two properties: the value of the associated eigenenergy (the lowest values usually describe dipolar modes, followed by quadrupole, hexapole modes, etc.) and the coupling strength to the external excitation.

For bigger particles, the determination of the complex eigenvalues and eigenvectors is more elaborate and can be calculated in terms of quasi-normal modes [46,47] or by applying the contour integral method [48,49]. Although the quasi-static approximation is still valid for a 150 nm cube, we find the quasi-normal modes [44] more convenient as they allow us to directly compute eigenmodes within a specific energy window, in contrast to the quasi-static approach where the separation of edge and face modes is considerably more cumbersome [50]. In our numerical Boundary Element Method (BEM) approach (see Eq. (21) in [51]), we calculated the eigenmodes of a 150 nm MgO cube which are shown in the Supplementary data online (Figs. S2 and S3). The corresponding eigenvalues are now distributed over the complex plane and the eigenmodes can be understood as a set of basis vectors describing the response of the system. The contribution of each mode is determined by the position of its eigenvalue (the closer it is to zero in the complex plane the more it contributes to the resonance) and the coupling strength between the specific mode and the external excitation. Although the full response for a 150 nm MgO cube is given by a linear combination of many eigenmodes, we can identify a few modes that contribute the most and whose spatial distribution agrees very well with the electron scattering maps at the corresponding loss energies for the corner, edge, and face resonance (see the Supplementary data online, Fig. S2). A more detailed analysis of the individual contributions of confined surface phonon eigenmodes to the scattering cross-section will be presented elsewhere. But, our results already show that in spite of the complexity of the numerous configurations only a few modes contribute to the vibrational scattering, in a similar manner as for confined surface plasmons [52,53].

To get further insight in the electron scattering from surface phonon modes within the dielectric approach, we calculated the surface charge densities and response electric fields at each resonance energy, for different probe locations. Figure 4 shows the modulus of the total induced electric field maps containing two insets: The upper left insets depict the surface charge density; and the lower left insets show the corresponding plane for which the field distribution has been computed. The position of the electron

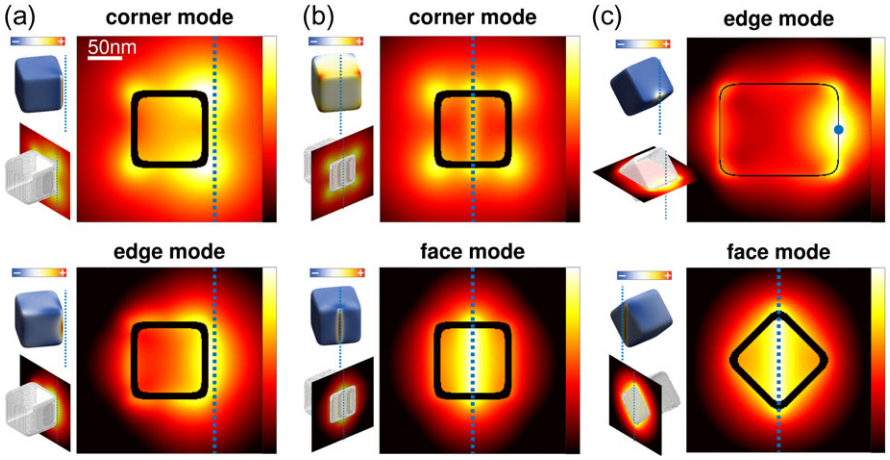

Fig. 4. Simulated response field intensity maps of a 150 nm MgO cube using a logarithmic colour scale. The main panels depict the total field intensities at certain cuts through the cube at the loss energies of the corner, edge, and face phonon modes, respectively. The two smaller insets on the left of each field map show the corresponding surface charge density maps (upper inset, scaled colormap) and the spatial orientation of the intersecting planes (lower insets) where the fields have been computed. The colour scale for the logarithmic field intensity plots ranges from $10^{-1.6}$ to $10^{0.6}$. The dotted lines mark the position of the exciting electron beam. In (a) the field maps are plotted in the [100] plane for an excitation 5 nm aloof from the cube corner. In (b) the electron beam is placed 5 nm aloof from the cube face and the fields are plotted in the [010] plane. Note that a fast electron can excite several modes when passing at a single location. In (c) the cube is tilted for 45° and the fields are plotted in the [011] and [100] plane (above and below, respectively) for a 5 nm aloof beam position.

beam in the plots is indicated by the dotted blue lines, and corresponds to an impact parameter of 5 nm.

In Fig. 4a, the electron beam is located close to the cube corner and the response field is plotted for two difference resonances: corner and edge modes. We find that the response field is strong at the corners and along the edge of the cube, and they are more prominent in regions closer to the electron trajectory. Also, note that the positive surface charges are strong at the corners and edges for each mode.

In Fig. 4b, the electron beam is positioned close to the cube face and the field intensity is plotted in the [100] plane for two resonances: corner and face modes. Notice in the upper plot that the corner mode is also obtained in spite of the fact that the electron beam is located between the corners. Also, in the lower plot we show that the coupling between the electron beam and the cube is strong across the whole face. Figure 4a and b illustrates that the fast electron can excite modes of different energies and consequently the scattering strength associated with each mode is driven by the impact parameter. In Fig. 4c, the cube is tilted by 45° ([110] orientation) and the probe is located close to the edge and face of the cube. In the upper plot, the edge mode is excited and the coupling between the nearby edge and the electron beam is strong. In the lower plot, the field is plotted for the face mode showing a strong dielectric response on the cube face, which suggests large cross section values for that location, in agreement with the experimental data shown in Fig. 3b.

A visual inspection of the response fields indicates that for each mode there is a typical pattern related to the mode which highlights certain regions of the cube. Also, the plot reveals that the induced fields extend away from the cube and decay slowly, verifying our expectation that dipole interactions produce surface phonon scattering over a large range of impact parameters (above 50 nm).

MgO nanocube on an amorphous SiO_2 substrate

In the previous sections, we described the existence of long-wavelength optical surface vibrational modes in *a*-SiO_2 films and MgO nanocubes, and their corresponding excitation using electron probes. Now, we bring both structures together and focus on the composite system consisting of an MgO cube placed on an *a*-SiO_2 substrate, the usual experimental setup of particles supported on films.

Figure 5 shows the calculated vibrational EELS scattering probabilities for a 30 nm MgO cube supported on an *a*-SiO_2 substrate. We simulated a 5 nm thick SiO_2 membrane of finite lateral size (90 nm) considering an experimentally determined dielectric function from [34] (Fig. 1b). This consideration provides further insights on the role of a dielectric substrate on the vibrational scattering than models modelling the substrate with a real value of dielectric permittivity. Interestingly, we find that the general influence of the thin *a*-SiO_2 substrate on the scattering spectra of the MgO cube is minor, so that the main peaks

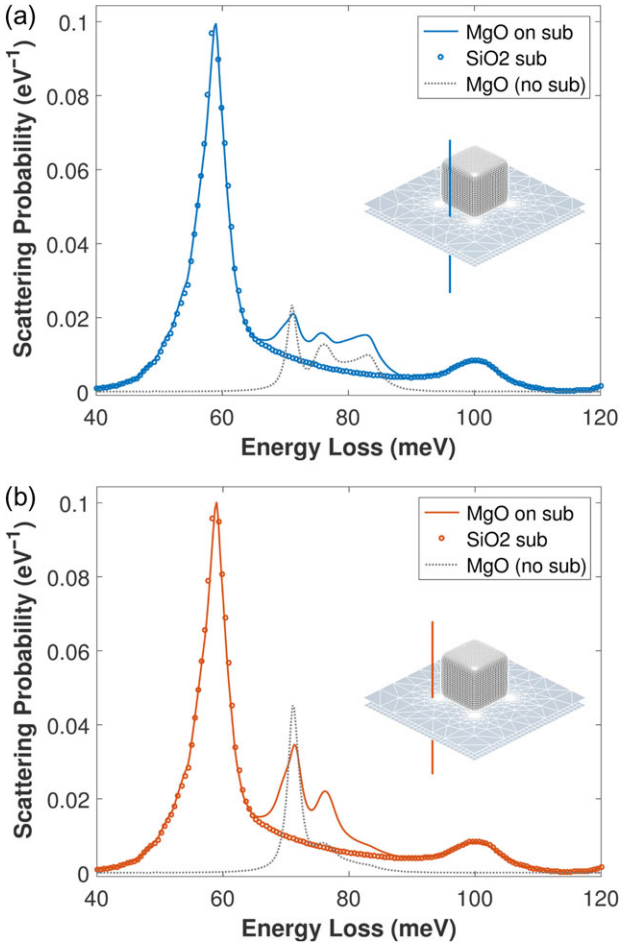

Fig. 5. Scattering probabilities for a 30 nm MgO cube placed on top of a 5 nm thick *a*-SiO_2 membrane. The solid line shows the loss spectra for certain beam positions. In (a) the beam is located close to the cube face and in (b) close to the cube corner, as indicated in the insets. The phonon scattering contribution coming from the SiO_2 substrate itself is indicated by the spherical symbols and the loss spectra for the cube without the substrate is plotted as grey dotted line. Note the substrate acts as a transparent material leaving the surface resonance of the cube (continuous curve) mostly unaffected.

corresponding to the corner, edge, and face resonances can still be recovered for the composite system. The additional absorption in SiO_2 leads to minor quenching of the cube resonances, but the corresponding energy shifts due to the modified dielectric environment are negligible (see dotted grey lines in Fig. 5). Note also that our results do not predict the appearance of a band splitting, typically obtained when the dielectric permittivity of a substrate is modelled using a finite value with null damping in plasmonic [54] and phononic [50] nanostructures.

Note also that in addition to the cube resonances, the two previously described optical vibrational resonances for *a*-SiO_2 at ~55 and 100 meV (TO_1 and TO_2, respectively) are clearly visible, but their scattering amplitude might be overestimated because of the finite substrate size. Therefore, our analysis shows that for thin silica substrates, the total response of the composite system can be approximately described as a simple addition of the cube and SiO_2 scattering contributions.

The absence of the band splitting in our results raises the question about the physical origin driving such absence. An analysis of the dielectric functions of the involved materials (Fig. 1) can shed light into the understanding of such effect. A visual comparison of the dielectric functions in Fig. 1a and b shows that the surface optical phonon excitations of MgO lies in a region (69–81 meV), where the dielectric function of the SiO_2 exhibits only finite positive contributions in both real and imaginary part. This indicates that at this condition of finite damping (Im[ε]) the substrate acts as a vacuum-like transparent element. To bring further physical insight into the origin of the transparency behaviour imposed by the substrate, we further analysed the effect of the substrate damping on the response of the whole system, considering the real part of the dielectric function as a finite constant (Re[ε] ~2.4), and the imaginary part as small values approaching to zero (Im[ε] → 0). Our results are shown in Fig. S4 and they indicated that at conditions of minor damping small resonances (band splitting) could develop in the region between the TO mode and the corner resonance (50–70 meV) of MgO [50]. This suggests that the transparency of the *a*-SiO_2 substrate might be driven by the characteristics of the damping process.

We also think that a more pronounced interaction should take place when the vibrational resonances of the particle energetically intersect with the surface phonon resonances of the substrate, probably producing strong coupling between surface vibrational modes. Thus, our studies suggest that one can explore the right combination of nanostructures and substrates (*a*-C, graphene, Si_3N_4, etc.) aiming to explore or avoid coupling effects. However, additional EELS experiments are needed to test theoretical predictions about the effects of substrate (material type and size) on the vibrational response of nanostructures.

Conclusions

We investigate experimentally and numerically the excitation of surface optical vibrational modes in an *a*-SiO_2 film and MgO nanocubes in the long-wavelength regime with keV electrons. We show that the vibrational surface response of these elementary phononic nanosystems can be explained by the dielectric characteristics of the involved materials in the dipole limit. We find that the surface optical vibrations are strongly constrained by the size and shape of the nanosystems. For the silica slabs, we find two EELS resonances as a result of the excitation of SPhP modes. Due to the geometry, the electron couples efficiently to the symmetric modes. For

the MgO cube, we find three surface optical phonon modes that are spatially concentrated at the corners, edges, and faces of the cube. These resonances can be described in terms of eigenmodes and the corresponding mode patterns can be resolved in the surface charge density distribution, as well as the response field intensity of the cube. We identify the few modes that determine the vibrational response of the system. We discuss the composite system of an MgO cube on top of a SiO_2 membrane, where the weak interaction between the two constituents suggests a transparent behaviour of the substrate at the energy range of the cube surface phonons.

Acknowledgements

M.J.L. and P.E.B. acknowledge the financial support of U.S. Department of Energy, Office of Science, Basic Energy Sciences under Award #DE-SC0005132. U.H. and A.T. acknowledge the financial support by the Austrian Science Fund FWF under project P27299-N27 and the SFB F49 NextLite (F4906-N23). U.H. and A. T. also thank G. Unger for helpful discussions regarding BEM eigenmodes. V.P.A. and L.C.F. acknowledge the financial support of the II-VI foundation and the Army Research Laboratory (programme coordinator Dr Aivars J. Lelis).

Supplemental data

Supplementary data are available at *Microscopy* online.

References

1. Ruppin R, and Englman R (1970) Optical phonons of small crystals. *Rep. Prog. Phys.* 33: 149–196.
2. Mills D L, and Burstein E (1974) Polaritons: the electromagnetic modes of media. *Rep. Prog. Phys.* 37: 817–926.
3. Ibach H, and Mills D L (1982) *Electron Energy Loss Spectroscopy and Surface Vibrations*, 1st edn, (Academic Press, New York).
4. Hillenbrand R, Taubner T, and Keilmann F (2002) Phonon-enhanced light–matter interaction at the nanometre scale. *Nature* 418: 159–162.
5. Shen S, Narayanaswamy A, and Chen G (2009) Surface phonon polaritons mediated energy transfer between nanoscale gaps. *Nano Lett.* 9: 2909–2913.
6. Maldovan M (2013) Sound and heat revolutions in phononics. *Nature* 503: 209–217.
7. Volokitin A I, and Persson B N J (2007) Near-field radiative heat transfer and noncontact friction. *Rev. Mod. Phys.* 79: 1291–1329.
8. Henkel C, Joulain K, Mulet J Ph, and Greffet J J (2004) Coupled surface polaritons and the Casimir force. *Phys. Rev. A.* 69: 023808.
9. Lagos M J, Trügler A, Hohenester U, and Batson P E (2017) Mapping vibrational modes in nanocubes. *Nature* 543: 529–532.
10. Caldwell J D, Lindsay L, Giannini V, Vurgaftman I, Reinecke T L, Maier S A, and Glembocki O J (2015) Low-loss, infrared and terahertz nanophotonics using surface phonon polaritons. *Nanophotonics* 4: 44–68.
11. Li N, Ren J, Wang L, Zhang G, Hänggi P, and Li B (2012) Phononics: manipulating heat flow with electronic analogs and beyond. *Rev. Mod. Phys.* 84: 1045–1066.
12. Narayanaswamy A, and Chen G (2003) Surface modes for near field thermophotovoltaics. *Appl. Phys. Lett.* 82: 3544–3546.
13. Fuchs R, and Kliewer K L (1965) Optical modes of vibration in an ionic crystal slab. *Phys. Rev.* 140: A2076–A2088.
14. Fuchs R, and Kliewer K L (1966) Optical modes of vibration in an ionic crystal slab including retardation. I. Nonradiative region. *Phys. Rev.* 144: 495–503.
15. Fröhlich H (1948) Theory of Dielectrics, (Oxford Unversity Press, Oxford).
16. Fuchs R (1975) Theory of the optical properties of ionic crystal cubes. *Phys. Rev. B* 11: 1732–1740.
17. Englman R, and Ruppin R (1966) Optical phonons in finite crystals. *Phys. Rev. Lett.* 16: 898–899.
18. Krivanek O L, Lovejoy T C, Dellby N, Aoki T, Carpenter R W, Rez P, Soignard E, Zhu J, Batson P E, Lagos M J, Egerton R F, and Crozier P A (2014) Vibrational spectroscopy in the electron microscope. *Nature* 514: 209–212.
19. Batson P E, and Lagos M J (2017) Characterization of misfit dislocations in Si quantum well structures enabled by STEM based aberration correction. *Ultramicroscopy* 180: 34–40.
20. Batson P E (1982) A new surface plasmon resonance in clusters of small aluminum spheres. *Ultramicroscopy* 9: 277–282.
21. Nelayah J, Kociak M, Stéphan O, de Abajo F J G, Tencé M, Henrard L, Taverna D, Pastoriza-Santos I, Liz-Marzán L M, and Colliex C (2007) Mapping surface plasmons on a single metallic nanoparticle. *Nat. Phys.* 3: 348–353.
22. Bosman M, Keast V J, Watanabe M, Maaroof A I, and Cortie M B (2007) Mapping surface plasmons at the nanometre scale with an electron beam. *Nanotechnology* 18: 165505.
23. Rez P, Aoki T, March K, Gur D, Krivanek O L, Dellby N, Lovejoy T C, Wolf S G, and Cohen H (2015) Damage-free vibrational spectroscopy of biological materials in the electron microscope. *Nat. Commun.* 7: 10945.
24. Dwyer C, Aoki T, Rez P, Chang S L Y, Lovejoy T C, and Krivanek O L (2016) Electron-beam mapping of vibrational modes with nanometer spatial resolution. *Phys. Rev. Lett.* 117: 256101.
25. Crozier P A, Aoki T, and Liu Q (2016) Detection of water and its derivatives on individual nanoparticles using vibrational electron energy-loss spectroscopy. *Ultramicroscopy* 169: 30–36.
26. Govyadinov A A, Konečná A, Chuvilin A, Vélez S, Dolado I, Nikitin A Y, Lopatin S, Casanova F, Hueso L E, Aizpurua J, and Hillenbrand R (2017) Probing low-energy hyperbolic polaritons in van der Waals crystals with an electron microscope. *Nat. Commun.* 8: 95.
27. Lambin Ph, Senet P, and Lucas A A (1991) Validity of the dielectric approximation in describing electron-energy-loss spectra of surface and interface phonons in thin films of ionic crystals. *Phys. Rev. B* 44: 6416–6428.
28. Gao W, Fujikawa Y, Saiki K, and Koma A (1993) Surface phonons of LiBr/Si(100) epitaxial layers by high resolution electron energy loss spectroscopy. *Solid State Commun.* 87: 1013–1015.
29. Fujikawara T, and Ohtaka K (1968) Energy loss of electron beam due to optical surface mode of vibration in a slab of NaCl-type ionic crystal. *J. Phys. Soc. Jpn* 24: 1326–1331.

30. Kroger E (1968) Berechnung der Energieverluste schneller Elektronen in dünnen Schichten mit Retardierung. *Z. Phys.* 216: 115–135.
31. Chen C H, Silcox J, and Vincent R (1975) Electron-energy losses in silicon: bulk and surface plasmons and Cerenkov radiation. *Phys. Rev. B* 12: 64–71.
32. Hohenester U, and Trügler A (2012) MNPBEM – a Matlab toolbox for the simulation of plasmonic nanoparticles. *Comput. Phys. Commun.* 183: 370–381.
33. García de Abajo F J (2010) Optical excitations in electron microscopy. *Rev. Mod. Phys.* 82: 209–275.
34. Palik E (1985) *Handbook of Optical Constants of Solids*. (Academic press, New York).
35. Hubner K (1977) Chemical bond and related properties of SiO2 (III). *Phys. Stat. Sol. (a)* 42: 501–509.
36. Innocenzi P (2003) Infrared spectroscopy of sol–gel derived silica-based films: a spectra-microstructure overview. *J. Non-Cryst. Solids* 316: 309–319.
37. Galeener F L (1979) Band limits and the vibrational spectra of tetrahedral glasses. *Phys. Rev. B* 19: 4292.
38. Ibach H (1979) Optical surface phonons in zinc oxide detected by slow-electron spectroscopy. *Phys. Rev. Lett.* 24: 1416–1418.
39. Oshima C, Aizawa T, Souda R, and Ishizawa Y (1990) Microscopic surface phonons of MgO (100) surface. *Solid State Commun.* 73: 731–734.
40. Burkel E, Seyfert C, Halcoussis Ch, Sinn H, and Simmons R O (1999) Phonon dispersion curves in *a*-SiO2 and hcp 3He and 4He determined by inelastic X-ray scattering. *Physica B* 263: 412–415.
41. Fuchs R, and Kliewer K L (1966) Optical modes of vibration in an ionic crystal slab including retardation. II. Radiative region. *Phys. Rev.* 150: 573–588.
42. Chen C H, and Silcox J (1979) Calculations of the electron-energy-loss probability in thin uniaxial crystals at oblique incidence. *Phys. Rev. B* 20: 3605–3614.
43. Lucas A A, and Vigneron J P (1984) Theory of electron energy loss spectroscopy from surfaces of anisotropic materials. *Solid State Commun.* 49: 327–330.
44. Makitalo J, Kauranen M, and Suuriniemi S (2014) Modes and resonances of plasmonic scatterers. *Phys. Rev. B* 89: 165429.
45. Hohenester U, and Trügler A (2008) Interaction of single molecules with metallic nanoparticles. *IEEE J. Sel. Top. Quant. Elect.* 14: 1430.
46. Ge R-C, Kristensen P T, Young J F, and Hughes S (2014) Quasinormal mode approach to modelling light-emission and propagation in nanoplasmonics. *New. J. Phys.* 16: 113048.
47. Alpeggiani F, D'Agostino S, Sanvitto D, and Gerace D (2016) Visible quantum plasmonics from metallic nanodimers. *Sci. Rep.* 6: 34772.
48. Asakura J, Sakurai T, Tadano H, Ikegami T, and Kimura K (2010) A numerical method for polynomial eigenvalue problems using contour integral. *Jpn. J. Appl. Math.* 27: 73–90.
49. Beyn W-J (2012) An integral method for solving nonlinear eigenvalue problems. *Lin. Alg. Appl.* 436: 3839–3863.
50. Lorenco-Martins H, and Kociak M (2017) Vibrational surface EELS probes confined Fuchs-Kliewer modes. arXiv:1707.09326.
51. García de Abajo F J, and Howie A (2002) Retarded field calculation of electron energy loss in inhomogeneous dielectrics. *Phys. Rev. B* 65: 115418.
52. Schmidt F, Ditlbacher H, Hohenester U, Hohenau A, Hofer F, and Krenn J R (2012) Dark plasmonic breathing modes in silver nanodisks. *Nano Lett.* 12: 5780.
53. Davis T J, and Gómez D E (2017) Colloquium: an algebraic model of localized surface plasmons and their interactions. *Rev. Mod. Phys.* 89: 011003.
54. Zhang S, Bao K, Halas N J, Xu H, and Nordlander P (2011) Substrate-induced fano resonances of a plasmonic nanocube: a route to increased-sensitivity localized surface plasmon resonance sensors revealed. *Nano Lett.* 11: 1657–1663.